# AN IMPROVED PARTICLE-BLADE INTERACTION MODEL TO INVESTIGATE TURBOMACHINERY EROSION NUMERICALLY

*Dionysios Klaoudatos (dionysios.klaoudatos@manchester.ac.uk)*

*Nicholas Bojdo (nicholas.bojdo@manchester.ac.uk)*

*Antonio Filippone (a.filippone@manchester.ac.uk)*

(Department of Mechanical, Aerospace and Civil Engineering (MACE), University of Manchester, Oxford Road, Manchester M13 9PL, UK)

*Stephen Covey-Crump (Stephen.J.Covey-Crump@manchester.ac.uk)*

*Merren Jones (merren.a.jones@manchester.ac.uk)*

*Alison Pawley (alison.pawley@manchester.ac.uk)*

(Department of Earth and Environmental Sciences (EES), University of Manchester, Oxford Road, Manchester M13 9PL, UK)

## ABSTRACT

**Gas turbine engine performance is severely degraded by solid particle (mineral dust, volcanic ash) ingestion. Current assessments of compressor performance degradation due specifically to erosion are heavily focused on the effects of quartz and volcanic glass ingestion but the components of mineral dusts have a much wider range of properties than are encompassed by these two materials. As a first step in developing a model of erosion that can be applied to more materials and to conditions outside those which have been experimentally investigated, we have incorporated a description of particle-blade interactions that is formulated in terms of relatively well-characterized material properties, into a Computational Fluid Dynamic (CFD) solver model of erosion of the blades in the NASA 37 rotor. Empirical erosion equations are also used to convert from particle impact to compressor rotor blade erosion rate. Running the model to simulate the erosive effect of the impact of 20-50 $\mu$m sized particles of corundum, quartz and silica glass for which experimental data exist, shows that it produces sensible values of erosion damage and sensible trends of erosion damage with changing particle size, density and hardness.**

## KEYWORDS

compressor blade, material properties, particle trajectories, erosion

 

## NOMENCLATURE

| | |
|---|---|
| $c$= chord [m] | $C_D$= drag coefficient |
| $c_s$= speed of sound [m/s] | $d$= diameter [m] |
| $E$= erosion rate [mg/g] | $E_{eff}$= effective Young's modulus [Pa] |
| $E_k$= kinetic energy (J) | $E_p$= particle Young's modulus [Pa] |
| $e$= particle CoR | $F$= force [N] |
| $H$= hardness [Pa] | $g$= acceleration due to gravity [m/s$^2$] |
| $K$= empirical constant | $K_{IC}$= fracture toughness [MPa.m$^{0.5}$] |
| $\dot{m}$= air mass flow rate [kg/s] | $N$= indentation hardness ratio |
| $P$= pressure [Pa] | $Pr$= pressure ratio |
| $Re$= Reynolds number | $\bar{s}$= flaw size [m] |
| $R$= blade span [m] | $r$= spanwise distance from blade hub (m) |
| $Tr$= temperature ratio | $T$= temperature [K] |
| $u$= velocity [m/s] | $x$= distance from blade leading edge [m] |
| $Y$= Yield strength [Pa] | |

Greek symbols

| | |
|---|---|
| $\alpha$= empirical constant | $\beta_1$= impact angle [deg] |
| $\dot{\epsilon}$= strain rate [1/s] | $\tau^+$= particle relaxation time |
| $\eta$= flaw density [m$^{-2}$] | $\eta_{c,eff}$= blade capture efficiency |
| $\mu$= dynamic viscosity [Pa.s] | $\mu_r$= impulse ratio |
| $\rho$= density [kg/m$^3$] | $\sigma_f$= brittle compressive strength [Pa] |
| $\Omega$= blade speed [rpm] | $\nu$= Poisson's ratio |

subscripts

| | |
|---|---|
| $C$= wall cutting | $D$= wall deformation |
| $i$= impact | $n$= normal component |
| $p$= particle | $R$= rebound |
| $t$= tangential | $w$= wall |
| $y$= plastic deformation region | 0= characteristic |
| $\tau$= friction | |

## INTRODUCTION

Dust ingestion into aeroengines is a significant concern for commercial and military aircraft operations over arid regions such as the Middle East and Africa. Large quantities of solid airborne particulates of varying size, mass concentration, and mineral and chemical composition are ingested by air-breathing engines causing degradation in gas turbine engine performance. The main degradation mechanisms are erosion of fan and compressor blades, deposition of particles on hot section components, corrosion, and blockage of cooling passages (e.g., Ghenaiet, 2016; Bons et al., 2017).

In the compressor, erosion is a particular concern because it causes changes to the blade shape, and increases surface roughness and tip clearance (Richardson et al, 1979). The extent and distribution of erosion is influenced by many parameters including the gas path, the engine operating conditions, the blade geometry, and factors affecting the nature of the blade-particle interaction, e.g., impact velocity, impact angle, particle size, particle shape, flow dynamic vis-

cosity, and the material properties of both blade and particles.

Several experimental studies have attempted to quantify the effect of factors that influence the blade-particle interaction on erosion of the engine substrate. Some have investigated the effect of particle size and impact velocity (e.g., Goodwin et al., 1969; Tabakoff et al., 1974), while others have shown that particle properties such as hardness (effectively, particle strength) and density have a strong influence on erosion (e.g., Tabakoff et al., 1979; Kotwal and Tabakoff, 1981). However, the range of materials investigated is very restricted in comparison with the range of naturally occurring dusts that may be ingested by engines (most data comes from quartz and fly ash particles), and given the complexity of the phenomena under investigation, the descriptions used to describe the experimental data tend to be primarily empirical rather than being physically-based. These matters are significant because they compromise the ability to apply the results to materials and engine conditions outside those directly examined in the experiments.

Examining erosion in a particular engine model is a two-step process. Firstly, the nature of the particle-blade interaction needs to be described, and secondly that interaction needs to be converted into an erosion-rate. Recent numerical studies using CFD tools to model particle motion through the turbomachinery blade passages and assess blade erosion (Ghenaiet, 2014; Ghenaiet, 2016) have used empirical correlations obtained from quartz and fly ash experimental data (Grant and Tabakoff, 1975; Tabakoff, 1989) for both of these steps. However, recently developed models by Uzi and Levy (2018; 2021) provide the opportunity to incorporate a more physically-based description for the particle-blade interaction part of the modelling. Their models explicitly include the material properties of particle and substrate (Young's modulus, Poisson's ratio, density, indentation hardness, yield strength) and hence, in principle, allow particle-blade interactions to be predicted for materials where these have not been obtained through direct experimentation.

In this paper we develop a CFD model for an axial-flow compressor rotor, the NASA Rotor 37, which incorporates Uzi and Levy's (2018) description of particle-blade interactions, with a modification to include the dependence of particle strength on impact velocity. The present model still requires the empirical equations developed by Grant and Tabakoff (1975) to convert from particle-blade interaction to erosion rate. With this in mind, we have applied the model to evaluate erosion caused by the impact of 20-50 $\mu$m sized particles of quartz (crystalline $SiO_2$), corundum (crystalline $Al_2O_3$) and silica glass (amorphous $SiO_2$) on annealed 2024 aluminium alloy, materials for which experimental erosion-rate data exists (Grant and Tabakoff, 1975; Tabakoff et al., 1979).

## BACKGROUND THEORY

This section outlines the key elements of the Uzi and Levy model (2018) relevant for this study as well as our modifications to their model. Their original model is based on a numerical study developed by other researchers (Wu et al., 2003) and it distinguishes three energy dissipation mechanisms: wall cutting $E_C$ (at low impact angles), wall deformation $E_{wD}$ (higher impact angles) and particle deformation $E_{pD}$. These three dissipation mechanisms are due to plastic deformation of both wall and particle. The normal component of the particle impact velocity $v_{ni}$ is used to calculate $E_{wD}$ and $E_{pD}$, whereas the tangential component $v_{ti}$ is used for the computation of $E_C$. The indentation hardness ratio $N$ (wall hardness to particle hardness) was considered as a criterion to quantify which mechanism (energy absorption by the wall or particle) is more dominant. The energy losses $E_{wD}$ and $E_{pD}$ are calculated from Eq. (1) and (2)

respectively

$$E_{wD} = N(1 - e_{n,w}^2)E_{k,ni} \tag{1}$$

$$E_{pD} = (1 - N)(1 - e_{n,p}^2)E_{k,ni} \tag{2}$$

where $E_{k,ni}$ is the normal component of particle impact kinetic energy and $e_{n,w}$ and $e_{n,p}$ are the normal coefficients of restitution (CoRs) due to the deformation of the wall and particle respectively, and are given by:

$$e_{n,w} = \begin{cases} 1 & , v_{y,w} > v_{n,i} \quad (elastic\,collision) \\ (\frac{v_{n,i}}{v_{y,w}})^{-0.091} & , 100 \geq \frac{v_{n,i}}{v_{y,w}} \quad (low\,plastic\,deformation\,region) \\ 2.08(\frac{v_{n,i}}{v_{y,w}})^{-0.25} & , \frac{v_{i,w}}{v_{y,w}} \geq \frac{v_{n,i}}{v_{y,w}} > 100 \quad (elastoplastic\,region) \\ 0.78(\frac{v_{n,i}}{v_{y,w}}\frac{Y_w}{E_{eff}})^{-0.5} & , \frac{v_{n,i}}{v_{y,w}} > \frac{v_{i,w}}{v_{y,w}} \quad (finite\,plastic\,region) \end{cases} \tag{3}$$

$$e_{n,p} = \begin{cases} 1 & , v_{y,p} > v_{n,i} \quad (elastic\,collision) \\ (\frac{v_{n,i}}{v_{y,p}})^{-0.091} & , 100 \geq \frac{v_{n,i}}{v_{y,p}} \quad (low\,plastic\,deformation\,region) \\ 2.08(\frac{v_{n,i}}{v_{y,p}})^{-0.25} & , \frac{v_{i,p}}{v_{y,p}} \geq \frac{v_{n,i}}{v_{y,p}} > 100 \quad (elastoplastic\,region) \\ 0.62(\frac{v_{n,i}}{v_{y,p}}\frac{\sigma_f}{E_{eff}})^{-0.5} & , \frac{v_{n,i}}{v_{y,p}} > \frac{v_{i,p}}{v_{y,p}} \quad (finite\,plastic\,region) \end{cases} \tag{4}$$

In Eq. (3) $Y_w$ is the wall yield strength and $E_{eff}$ is the effective Young's modulus (Uzi and Levy, 2018, their Eq. 18) of wall and particle. The variables $v_{y,w}$ and $v_{i,w}$ are the threshold impact velocities at which deformation of the wall begins that is characterized by microplastic (small deformations with limited plasticity) and finite plastic (deformation with significant plasticity) responses respectively (Uzi and Levy, 2018), and $\rho_w$ is the wall material density.

In Eq. (4) $v_{y,p}$ and $v_{i,p}$ are the threshold impact velocities at which microplastic and finite plastic deformation of the particle begins and are calculated from Eq. (5) and (6)

$$v_{y,p} = 5.052(\frac{{\sigma_f}^5}{E_{eff}^4\rho_p})^{0.5} \tag{5}$$

$$v_{i,p} = 0.008v_{y,p}(\frac{E_{eff}}{\sigma_f})^2 \tag{6}$$

where $\rho_p$ is particle density.

We apply two modifications to the Uzi and Levy model. First, the strength of the particles at the impact velocities of interest is very sensitive to how fast they are deformed (e.g., Whitaker and Bons, 2018). To accommodate this we have replaced $\sigma_f$ in Eq. (4) with an expression that accommodates the strain-rate dependence of $\sigma_f$. In the absence of well-constrained descriptions of the yield strength at the strain-rates of interest for the materials we are using, we use an expression for the strain-rate dependence of brittle compressive strength which has been shown to be applicable for a large number of materials (Kimberley et al., 2013),

$$\frac{\sigma_f}{\sigma_0} = 1 + \left(\frac{\dot{\epsilon}}{\dot{\epsilon}_0}\right)^{2/3} \tag{7}$$

where strain rate depends on particle impact velocity and is given from Roisman and Tropea (2015)

$$\dot{\epsilon} = \frac{2v_i^2 \rho_p^{0.5}}{d_p \sigma_0^{0.5}} \tag{8}$$

The variables $\sigma_0$ and $\dot{\epsilon}_0$ are the characteristic stress and characteristic strain rate respectively, as calculated from

$$\sigma_0 = \frac{\alpha K_{IC}}{\overline{s}\eta^{1/4}} \tag{9}$$

$$\dot{\epsilon}_0 = \frac{2\sigma_0^3 c_s}{K_{IC}^2 E_{eff}} \tag{10}$$

where $\alpha$=10 is an empirical constant, $\overline{s}$ is the flaw size (here assumed equal to the particle size), $\eta$ is the flaw density (number of flaws per particle area, here assumed as one flaw per particle) and $c_s$ is the speed of sound,

$$c_s = \sqrt{\left(\frac{E_p}{\rho_p}\right)\left(\frac{1-\nu_p}{(1-2\nu_p)(1+\nu_p)}\right)} \tag{11}$$

where $E_p$ is the particle Young's modulus and $\nu_p$ is particle Poisson's ratio (Kimberley et al., 2013; Hogan et al., 2016). At the strain rates of interest we are not expecting the difference between the brittle compressive strength and the plastic yield strength to be greater than current uncertainties on what the values of these properties are for our materials at high strain rates.

The original model of Uzi and Levy calculates the variable $e_{n,p}$ by considering a constant particle yield strength at each particle impact instead of using the $\sigma_f$. The increase of $\sigma_f$ with $\dot{\epsilon}$ results in an increase of particle yield velocity, $v_{y,p}$ which means smaller particle deformation. The sensitivity of $v_{y,p}$ on $\sigma_f$ is different for each particle, because $v_{y,p}$ also depends on effective Young's modulus and particle density, but we found that the Uzi and Levy model (2018) over-estimated the plastic deformation of quartz particles by 58% at impact velocities higher than 333 m/s.

The total normal CoR $e_{n,total}$ due to normal deformation of wall and particle is calculated as in the Uzi and Levy (2018) model as

$$e_{n,total} = \sqrt{1 - \frac{E_{wD} + E_{pD}}{E_{k,ni}}} \tag{12}$$

The second modification we have applied to the Uzi and Levy model refers to the calculation of the tangential energy loss $E_C$. The equation used by Uzi and Levy to estimate wall tangential CoR $e_t$ contains several empirical constants and so to avoid these a simpler relation proposed by Bons et al. (2017) is used instead. We ignore the tendency for adhesion of the particle to the surface because Bons et al. (2017) consider it is only important for particle sizes smaller than 10 $\mu$m. Therefore, the tangential rebound velocity $v_{t,R}$ and $e_t$ are calculated as

$$v_{t,R} = v_{t,i} - \mu_r v_{n,i}(1 + e_{n,total})\cos^2(\beta_1) \tag{13}$$

$$e_t = \sqrt{\frac{E_{k,tR}}{E_{k,ti}}} \tag{14}$$

where $\mu_r$ is the impulse ratio, assumed here to be constant ($\mu_r$=0.3).

## METHODOLOGY

A single blade passage of the NASA Rotor 37 is used as case geometry to simulate particle trajectories for the present work. The rotor geometry was taken from the study of Reid and Moore (1978). Experimental data for the rotor aerodynamic performance are also provided in their report. The design characteristics and its design operating conditions are summarized in Table 1.

Table 1: Design configurations and operating conditions

| Geometry | NASA Rotor 37 |
|---|---|
| Number of blades | 36 |
| Blade span ($R$) | 79.11 mm |
| Chord length at the tip ($c$) | 56 mm |
| Aspect ratio | 1.19 |
| Solidity | 1.3 |
| Tip clearance | 0.356 mm |
| Rotating speed ($\Omega$) | 17188 rpm |
| Pressure ratio ($Pr$) | 2.056 |
| Mass flow rate ($\dot{m}$) | 20.2 kg/s |
| Temperature ratio ($Tr$) | 1.27 |

### Numerical grid

A hexahedral grid with a total number of 1,074,064 cells was generated to carry out the CFD simulations. The mesh was refined near the leading and trailing edges of the blade, near the hub and shroud, and in tip clearance. The values of $y^+$ are within 5-70 near the walls. Particles are injected from the inlet surface, which consists of 2193 elements. The size of the elements is the same to ensure a uniform particle injection.

### Three-dimensional gas phase flow and turbulence modelling

The numerical simulations were performed in a steady frame motion by using the commercial CFD solver ANSYS FLUENT 19.2 (ANSYS FLUENT, 2019). The 3D Reynolds-averaged Navier Stokes (RANS) equations were solved using a finite volume method. The density-based solver with an implicit Roe-Flux-difference splitting (FDS) linearization of the governing equations was adopted. A Green-Gauss node based spatial discretization and a second order Upwind scheme for the flow were chosen.

The realizable k-$\epsilon$ turbulence model with a Standard Wall Function (STW) was applied. A first order Upwind scheme was selected to solve the turbulence terms. With the use of k-$\epsilon$ STW model, there is an isotropic treatment of the turbulence near the wall. This means that when the value of $y^+$ becomes less than 5, turbulence kinetic energy will be overestimated (Tian and Ahmadi, 2006). In this work, values of $y^+$ are always higher than 5, as mentioned above.

In their study, Tian and Ahmadi also evaluated the relationship between the turbulence models and non-dimensional particle relaxation time $\tau^+$, which is defined as

$$\tau^+ = \frac{\rho_p d_p^2 u_\tau^2}{18\rho\nu} \tag{15}$$

where $\rho_p$ is particle density, $d_p$ is particle diameter, $u_\tau$ is the flow shear velocity, $\rho$ is air density and $\nu$ is air kinematic viscosity. Tian and Ahmadi (2006) found that the k-$\epsilon$ STW turbulence model overpredicts particle impact velocity in a Brownian ($0 < \tau^+ < 10^{-2}$) and transition ($10^{-2} < \tau^+ < 10$) region. For the inertial ($\tau^+ > 10$) region, the k-$\epsilon$ STW turbulence model overpredicts particle impact velocity in a minor way compared with the other regions. In this study, $\tau^+$ is in the range of 14.5-163, hence the k-$\epsilon$ STW turbulence model was considered reliable to investigate near-wall particle behaviour.

**Boundary conditions**

The total pressure and total temperature were imposed at the inlet boundary with respective values $P_{1,t}$=101.325 kPa and $T_{1,t}$=288.15 K. Turbulent intensity of 5% and viscosity ratio of 10 were imposed as turbulent boundary conditions at the inlet. The average static pressure was imposed at the outflow boundary. The value of the average static pressure ranged from 108 kPa to 120 kPa in order to estimate the rotor pressure ratio at various air mass flow rates. Rotational periodic boundary conditions were applied to the lateral surfaces of the computational domain. All the simulations were carried out at the design rotational speed 17188 rpm.

**Validation for the airflow**

The simulated air flow of the present study is compared with the experimental data of Reid and Moore (1978) and the numerical results of Suman et al. (2014) in Fig. 1. Two grids (with 570316 and 1074064 cells) were used to prove the mesh independence of the results. Although the present numerical model underestimates the blade performance slightly, the shape of the rotor performance map was correctly reproduced by both grids. The grid with 1074064 cells was chosen for the next simulations because it gives good results at reasonable computational cost and consists of a larger number of particles at the inlet surface.

**Balance of forces on particles**

The Eulerian-Lagrangian approach was implemented to model the kinematic behaviour of the ingested particles. The gas phase is treated as a continuum and it is solved first, while the dispersed phase is computed by tracking a sufficient number of particles through the converged air flow field. This approach is more economical than the Eulerian-Eulerian and provides very accurate results (Ghenaiet, 2014).

Particle motion is determined by integrating a force balance equation on the particle, which is given by Eq. (16):

$$\frac{du_p}{dt} = F_D + \frac{g\left(\rho_p - \rho\right)}{\rho_p} + F + F_S + F_B \tag{16}$$

where $u_p$ is the particle velocity, $F_D$ is the drag force per unit particle mass, $g$ is the acceleration due to gravity and $F$ represents the contribution of additional forces (e.g, forces which act on particles due to blade rotation). The gravity term was not taken into account in the present study. Saffman's lift $F_s$ and Brownian $F_B$ forces were not considered as well, because their effects are

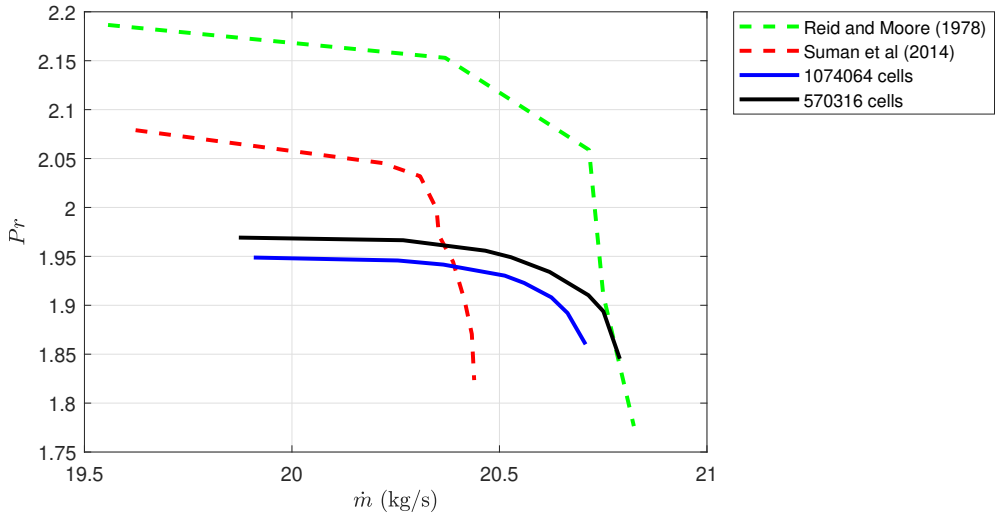


Figure 1: **Comparison of the pressure ratio ($Pr$) obtained at different air mass flow rates ($\dot{m}$) from the CFD modelling with experimental and numerical data in the literature (Reid and Moore, 1978; Suman et al., 2014)**

significant for sub-micron particles only. The term $F$ incorporates forces which act on particles due to blade rotation.

In this work, particles are assumed to be spherical. Thus, the drag force per unit particle mass is obtained from Eq. (17)

$$F_D = \frac{18\mu}{\rho_p d_p^2}\frac{C_D Re_p}{24}(u - u_p) \tag{17}$$

where $u$ is the air velocity, the drag coefficient $C_D$ is calculated by the equation of Morsi and Alexander (1972) and $\mu$ is the fluid dynamic viscosity. $Re_p$ is the particle Reynolds number given from Eq. (18)

$$Re_p = \frac{\rho d_p |u_p - u|}{\mu} \tag{18}$$

**Tracking method and particle injection**

In this numerical study, the stochastic Discrete Random Walk (DRW) model was used to model particle dispersion in the fluid phase. With this approach, the mean fluid phase velocity is used to determine the mean path of the particles, while the fluctuating gas velocity is applied to determine the turbulent dispersion of each particle from the mean trajectory.

All the particles were injected from the inlet surface with the same velocity as the air flow (170 m/s). The sensitivity of the results to the number of injected particles was investigated by re-running the model for 25000, 50000, and 150000 injected particles (all 20 $\mu$m in diameter in this sensitivity analysis), for each material (quartz, corundum and silica glass). The blade capture efficiency $\eta_{c,eff}$ (ratio of particles that hit the blade to the injected particles) was calculated. The results along with the particle material properties are shown in Table 2 ($H_p$ is particle hardness and $K_{IC}$ is particle fracture toughness). The difference in blade capture efficiency between 25000 and 50000 particles was only 0.1% (= 6170 particles). This difference

is not sufficiently significant to warrant the additional computational cost of simulating more particle trajectories. Therefore, we chose to use 25000 particles. One-way coupling (fluid phase is not affected by the dispersed particles) was implemented since the particle volume fraction was very low ($\ll$10%). All particles were dispersed in a converged air flow field at the best efficiency point of the compressor.

Table 2: Injection independence study and particle properties

| | $\eta_{c,eff}$ 25000 particles | $\eta_{c,eff}$ 50000 particles | $\eta_{c,eff}$ 150000 particles | $\rho_p$ (kg/m$^3$) | $H_p$ (GPa) | $E_p$ (GPa) | $\nu_p$ | $d_p$ ($\mu$m) | $K_{IC}$ (MPa$\sqrt{m}$) |
|---|---|---|---|---|---|---|---|---|---|
| quartz | 0.2436 | 0.2452 | 0.2442 | 2650 | 11 | 96.47 | 0.076 | 20 | 0.715 |
| corundum | 0.3112 | 0.3121 | 0.3118 | 3950 | 20 | 360 | 0.22 | 20 | 2.774 |
| glass | 0.221 | 0.2219 | 0.2215 | 2210 | 6.276 | 72.52 | 0.1731 | 20 | 0.521 |

**Particle-walls impact behaviour**

Different Discrete Phase Modelling (DPM) conditions were implemented for the three wall boundaries (blade, hub and shroud) of the domain. A specific function was created to capture the particle impact angle, positions and velocities on the blade surface. The blade surface was also divided into 6 strips (13%, 27%, 42%, 58%, 76%, 94% of the span) so that particle impacts could be also analyzed in the spanwise direction of the blade. The definition of the distance between impacting particle and blade leading edge (LE) along the chord, and three representative blade strips are illustrated in Fig. 2. The trajectory of each particle was terminated when it hit the blade, thus only their first impact was considered to calculate the erosion.

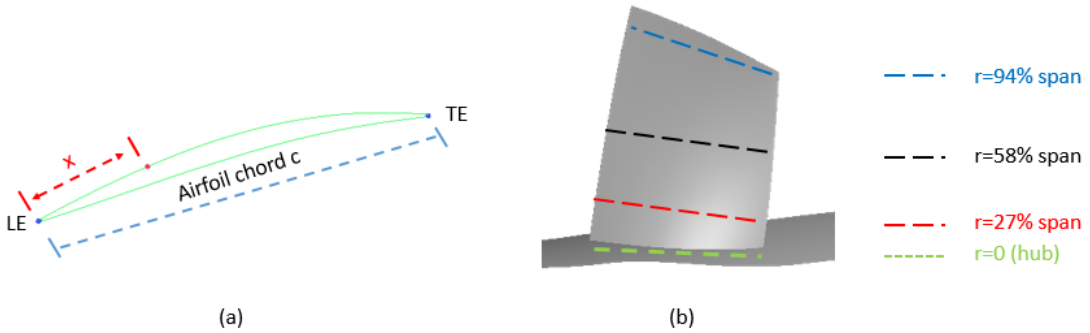


Figure 2: **(a) Distance of impacting particle from airfoil leading edge along the chord, (b) Spanwise division of the blade**

Reflect (particle bouncing) DPM conditions were imposed to predict the particle rebound behaviour from the rotor hub and shroud. Eq. (12) and (14) were applied to determine particle CoRs after their impact on blade, hub and shroud.

**Model for erosion estimation**

The empirical model developed by Grant and Tabakoff (1975) was used to predict blade erosion $E$, which is expressed as the amount of material removed (mg) per unit mass (g) of impacting particles.

$$E = K_1 f(\beta_1) v_i^2 \cos^2 \beta_1 (1 - e_t^2) + K_3 (v_i \sin \beta_1)^4 \tag{19}$$

$$f(\beta_1) = 1 + CK(K_2 \sin \frac{90}{\beta_0}\beta_1) \tag{20}$$

$$CK = \begin{cases} 1 & \beta_1 \leq \beta_o \\ 0 & \beta_1 > \beta_o \end{cases} \tag{21}$$

This erosion model was derived from the impact of solid particles on an 2024 aluminum alloy blade. It is probably also applicable to other metal blades (titanium, inconel, stainless steel), but with different values for the constants $K_1$, $K_2$ and $K_3$.

For quartz the values $K_1$=3.67x10$^{-6}$, $K_2$=0.585 and $K_3$=6x10$^{-12}$ were obtained from the study of Grant and Tabakoff (1975), whereas $K_1$=1.56988x10$^{-6}$, $K_2$=0.3193 and $K_3$=2x10$^{-12}$ were found from the experiments of Tabakoff et al. (1979) for silica glass. The empirical constants for corundum were calculated as $K_1$=2.657x10$^{-5}$, $K_2$=0.3502 and $K_3$=1.35x10$^{-11}$ after applying curve fitting on the experimental results of Tabakoff et al. (1979). In Eq. (20) and (21) $\beta_0$=20° is the impact angle for maximum erosion (Grant and Tabakoff, 1975).

## RESULTS AND DISCUSSION

Erosion patterns, as predicted from the impingement of the different particles with sizes 20-50 $\mu$m along the chord and span of the blade, are illustrated in Fig. 3-5. Each dot on the graph represents an impacting particle on the blade. Different erosion rates are found at the same impact position (mainly at x/c<50%) for a given particle type because some of the particles hit these blade positions directly at high velocity (up to 350 m/s), while others hit them at lower velocity (down to 50 m/s) because they hit them after rebound from the shroud (on the suction side) or from the hub (on the pressure side). Near the hub, particle impact velocity is in the range 295-320 m/s.

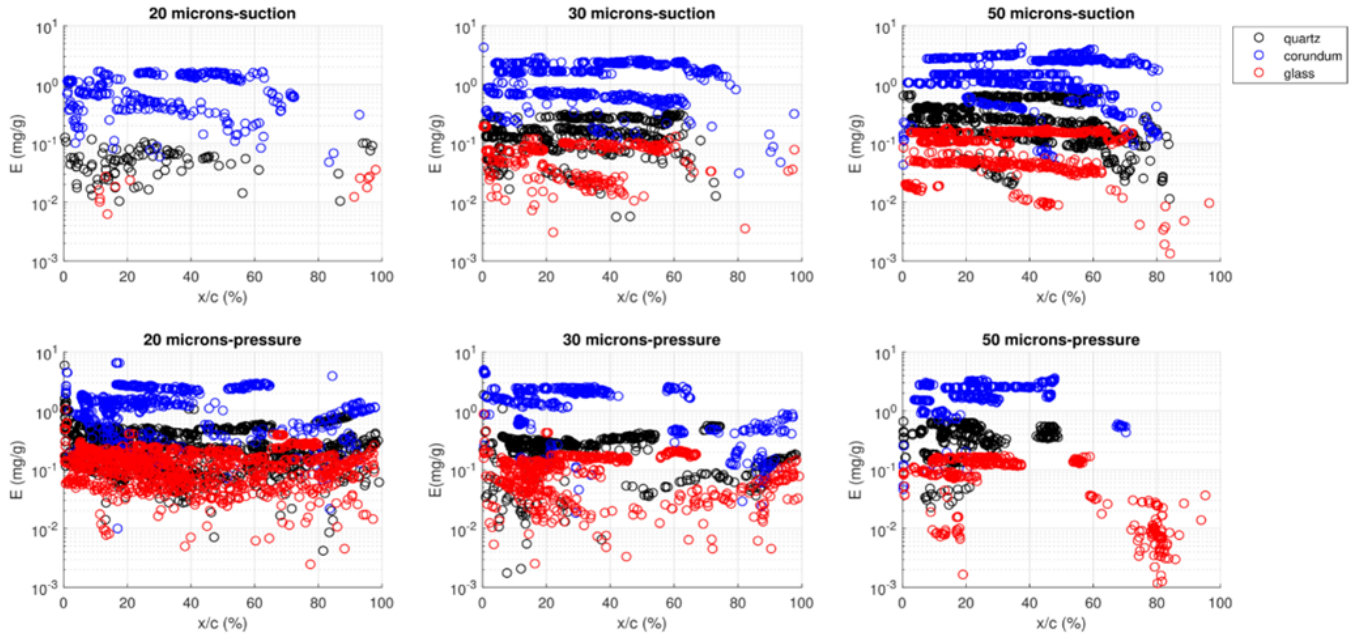


Figure 3: **Erosion rate caused by different particles with various sizes along the chord on the suction and pressure side of the blade tip (94% of blade span)**

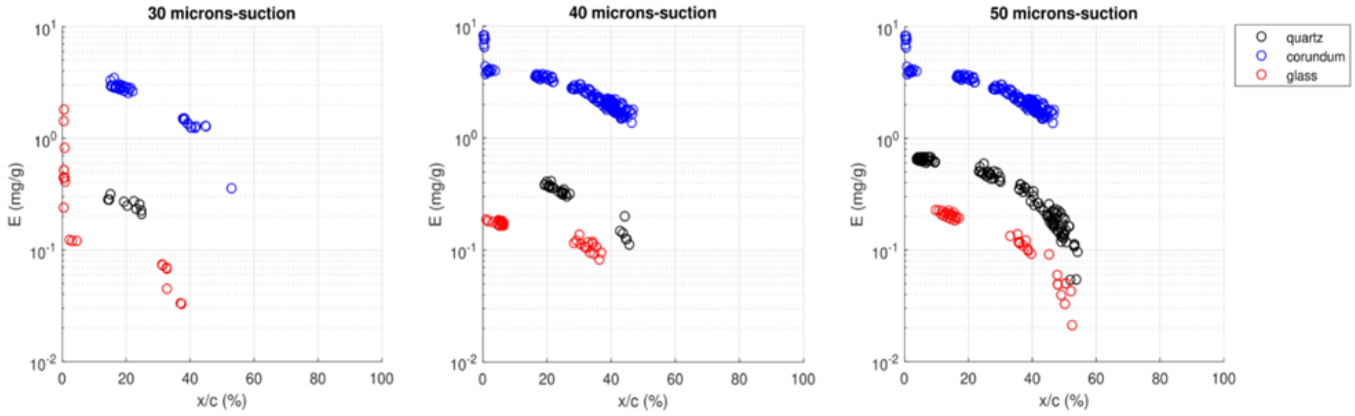


Figure 4: **Erosion rate caused by different particles with various sizes along the chord on the suction side of the blade midspan (58% of blade span)**

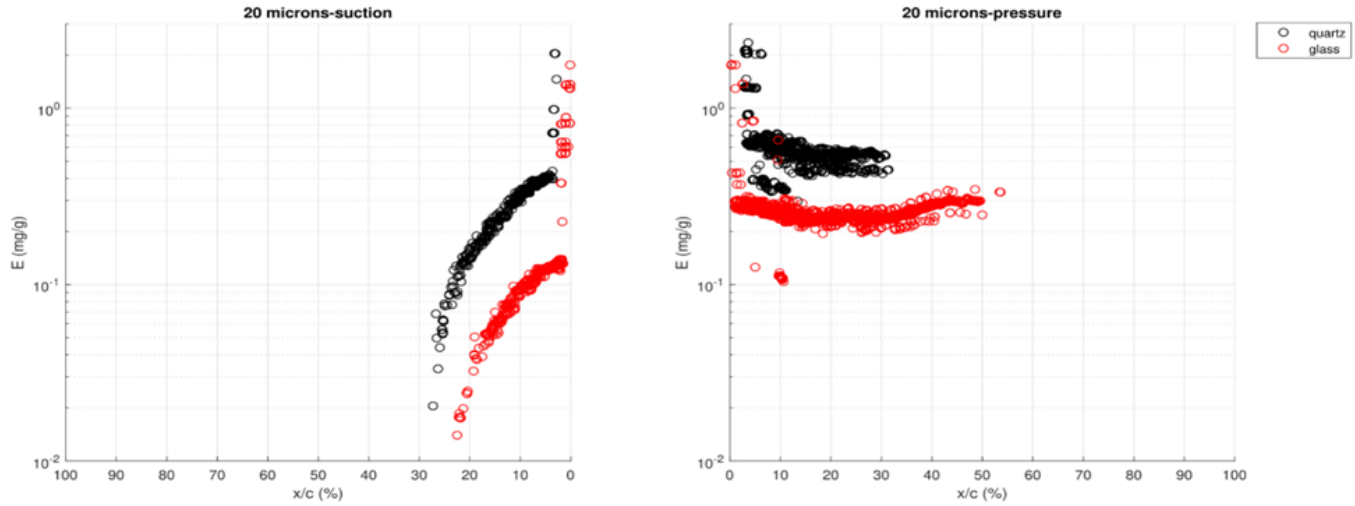


Figure 5: **Erosion rate caused by quartz and glass particles with 20 $\mu$m along the chord on the suction (left graph) and pressure (right graph) side of the blade strip near the hub**

As can be seen by comparing Figs 3, 4 and 5, the number of particle impacts is much greater towards the blade tip (Fig. 3). This is due to the centrifugal force. The centrifugal force increases significantly with increasing particle size and density, so that on the blade strip near the hub (Fig. 5) only the smallest particles (20 $\mu$m) in the lowest density materials (quartz and silica glass) impacted the blade. Corundum caused significantly higher erosion damage than that of quartz and glass, due to its extremely high hardness and higher density. The blade LE is severely eroded for all impacts.

Particle impact velocity and hence erosion rate are affected by fluid flow phenomena. Erosion rate on the suction side of the midspan (Fig. 4) and near the hub (Fig. 5) drops immediately after the blade LE due to airflow separation, which results in smaller particle impact velocities. Airflow separation also decreases the erosion on the suction side of the blade tip at the rear part of the chord (x/c>60%). However, it is also noticed that despite the flow separation, few particles cause high amount of erosion near the trailing edge (TE) of the blade tip suction side.

These particles are dragged from the pressure side through the tip leakage vortex, due to the blade tip gap.

## CONCLUSIONS

We have developed a CFD model to assess the erosion rate of blades within an axial-flow compressor rotor (NASA rotor 37) that is caused by ingested dust particles. We have incorporated a description of particle-blade interactions which describes the energy dissipation arising from these interactions in terms of well characterized material properties (Uzi and Levy, 2018) but have retained existing empirical descriptions (Grant and Tabakoff, 1975) to convert this energy dissipation into erosion rate.

For corundum, quartz and silica glass particles we are able to reproduce the key findings obtained from previous modelling work that used experimental data to describe particle-blade interactions for these particles, namely that blade erosion damage increases with particle size, and that it shows a similar sensitivity to particle density and hardness as that observed in the experiments on these materials. For the blades in the NASA rotor 37, erosion damage is predicted to be much greater on the leading edge of the blades than on the trailing edge.

The use of Uzi and Levy's description of particle-blade interactions enhances the potential of the model to be applied outside the conditions under which these interactions have been experimentally investigated, and also allows the model to be applied to a much wider range of dust materials than have been so far examined experimentally. In future simulations, we will seek to use the description of particle-blade interactions to extend particle tracking beyond first impact. However, the reliance upon experimental data to convert impact energy dissipation into erosion rates highlights the need for a more general model that is able to accommodate the wide range of minerals that have been identified in aircraft gas turbine engines.

## REFERENCES


ANSYS, 2019, ANSYS FLUENT User Manual, ANSYS, Inc., Canonsburg, PA.

Bons, J. P., Prenter, R., and Whitaker, S. (2017). 'A Simple Physics-Based Model for Particle Rebound and Deposition in Turbomachinery', ASME Journal of Turbomachinery, 139(8).

Ghenaiet, A. (2016). 'Modeling of Particle Trajectory and Erosion of Large Rotor Blades', International Journal of Aerospace Engineering, 2016.

Ghenaiet, A. (2014). 'Study of particle ingestion through two-stage gas turbine', Proceedings of ASME Turbo Expo 2014: Turbine Technical Conference and Exposition, Dusseldorf, Germany, June 16-20, 2014.

Goodwin J. E, Sage, W. and G. P. Tilly. (1969). 'A study of erosion by solid particles', Proceedings of the Institute of Mechanical Engineers, 184, pp. 279-292

Grant, G., and Tabakoff, W. (1975). 'Erosion prediction in turbomachinery resulting from environmental solid particles,' AIAA Journal of Aircraft, 12(5), pp. 471-478.

Hogan, J. D., Farbaniec, L., Daphalapurkar, N. and Ramesh, K. T. (2016). 'On Compressive Brittle Fragmentation', Journal of the American Ceramic Society, 99(6), pp.2159-2169.

Hussein, M. F., and Tabakoff, W. (1973). 'Dynamic behavior of solid particles suspended by polluted flow in a turbine stage', Journal of Aircraft, 10(7), pp. 434-440.

Kimberley, J., Ramesh, K. T. and Daphalapurkar, N. P. (2013). 'A scaling law for the dynamic strength of brittle solids', Acta Materialia, 61(9), pp.3509-3521.

Kotwal, R. and Tabakoff, W. (1981). 'A New Approach for Erosion Prediction Due To Fly Ash', Journal of Engineering for Power, 103(2), pp.265-270.

Morsi, S. A., and Alexander, A. J. (1972). 'An Investigation of Particle Trajectories in Two-Phase Flow Systems', Journal of Fluid Mechanics, 55(2), pp. 193-208.

Paliwal, B. and Ramesh, K. T. (2007). 'Effect of crack growth dynamics on the rate-sensitive behavior of hot-pressed boron carbide', Scripta Materialia, 57(6), pp.481-484.

Reid, L., and Moore, R. D. (1978). 'Design and Overall Performance of Four Highly-Loaded, High-Speed Inlet Stages for an Advanced High-Pressure-Ratio Core Compressor', NASA Lewis Research Center, Cleveland, OH, NASA Report No. TP 1337.

Richardson, J. H., Sallee, G. P., and Smakula, F. K. (1979). 'Causes of High Pressure Compressor Deterioration in Service', AIAA Paper 79-1234.

Roisman, I. V., and Tropea, C. (2015). 'Impact of a crushing ice particle onto a dry solid wall', Proceedings of the Royal Society A, 471:20150525.

Suman, A., Kurz, R., Aldi, N., Morini, M., Brun, K., Pinelli, M. and Ruggero Spina, P. (2014). 'Quantitative Computational Fluid Dynamics Analyses of Particle Deposition on a Transonic Axial Compressor Blade-Part I: Particle Zones Impact', Journal of Turbomachinery, 137(2), p. 021009.

Tabakoff, W., (1989). 'Measurements of Particles Rebound Characteristics on Materials Used in Gas Turbines', AIAA $24^{th}$ Thermophysics Conference, Buffalo, New/York/June 12-14, 1989.

Tabakoff, W., Kotwal, R. and Hamed, A. (1979). 'Erosion study of different materials affected by coal ash particles', Wear, 52(1), pp.161-173.

Tabakoff, W., Grant, G., and Ball, R. (1974). 'An Experimental Investigation of Certain Aerodynamic Effects on Erosion', AIAA $8^{th}$ Aerodynamic Testing Conference, Bethesda, Maryland, July 8-10, 1974.

Tian, T., and Ahmadi, G. (2006). 'Particle Deposition in Turbulent Duct Flows-Comparisons of Different Model Predictions', Journal of Aerosol Science, 38(4), pp.377-397.

Uzi, A., and Levy, A. (2021). 'Energy absorption in particle breakage under impact load', Powder Technology, 377, pp.308-323.

Uzi, A., and Levy, A. (2018). 'Energy absorption by the particle and the surface during impact', Wear, 404-405, pp.92-110.

Whitaker S. M., and Bons J. P. (2018). 'An improved particle impact model by accounting for rate of strain and stochastic rebound', Proceedings of ASME Turbo Expo 2018: Turbomachinery Technical Conference and Exposition, Oslo, Norway, June 11-15, 2018.

Wu, C., Li, L. and Thornton, C. (2003). 'Rebound behaviour of spheres for plastic impacts', International Journal of Impact Engineering, 28(9), pp.929-946.